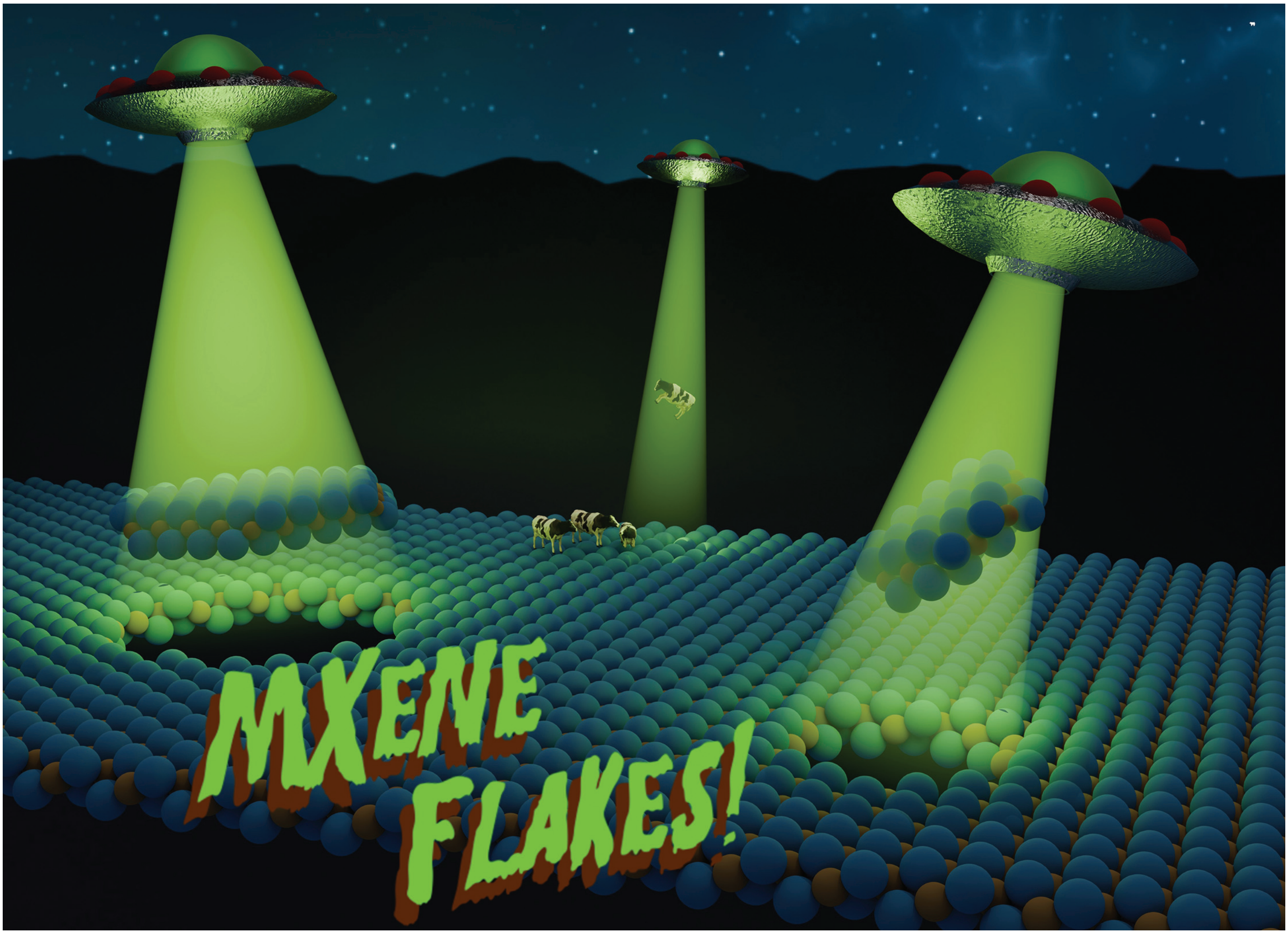

Showcasing research from Prof. Morales-García et al. at Computational Materials Science Laboratory (CMSL), University of Barcelona, Barcelona, Spain.

Cutting edge(s): towards realistic modelling of MXene flakes

Modelling of Ti_2C MXene flakes is carried out using top-down Wulff construction procedure. By means of the density functional theory, changes in the structural, energetic, electronic and magnetic properties are explored as a function of the composition and the MXene flake dimension.

Image reproduced by permission of Ángel Morales-García from *Nanoscale*, 2025, **17**, 22849.

As featured in:

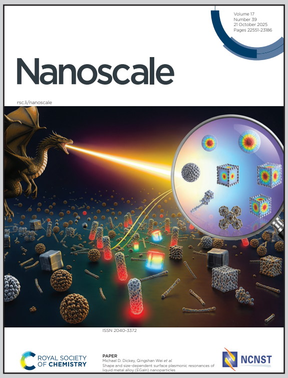

See Ángel Morales-García *et al.*, *Nanoscale*, 2025, **17**, 22849.

ROYAL SOCIETY
OF **CHEMISTRY**

rsc.li/nanoscale

Nanoscale

ROYAL SOCIETY OF CHEMISTRY

PAPER

View Article Online
View Journal | View Issue

Check for updates

Cite this: *Nanoscale*, 2025, **17**, 22849

Cutting edge(s): towards realistic modelling of MXene flakes

Néstor García-Romeral, Ángel Morales-García, * Francesc Viñes and Francesc Illas

We investigate the structural, energetic, electronic, and magnetic properties of newly designed and realistic Ti_2C MXene flake models using density functional theory (DFT) calculations. By means of the Wulff construction procedure, we model flakes that closely resemble experimentally synthesized structures, exhibiting a hexagonal morphology dominated by the thermodynamically stable $(11\bar{2}0)$-nonpolar surface. As the flake size increases, structural parameters and relative stability converge toward periodic Ti_2C slab behaviour, with diminishing quantum confinement (QC) effects. Electronic structure calculations reveal a gapless nature across all sizes, with negligible QC effects on optical properties, even under different magnetic configurations. Hybrid HSE06 calculations predict a slight increase in the band gap compared to the PBE functional, yet this gap vanishes in larger flakes, aligning with periodic slab behaviour, while the band edge energy decreases as the flake size increases. Spin-polarized calculations confirm an antiferromagnetic (AFM) ground state for all flakes, with energy differences between the AFM, nonmagnetic (NM), and ferromagnetic (FM) states increasing with increasing size. Notably, for smaller $(Ti_2C)_n$ flakes ($n < 90$), AFM and FM configurations are nearly degenerate, whereas for larger flakes ($n \geq 90$), AFM becomes the definitive ground state. Functionalization of the basal plane with oxygen stabilizes Ti_2CO_2 flakes, inducing structural edge bending, suppressing magnetism, and favouring an NM ground state. The band gaps in functionalized flakes exhibit size-dependent narrowing due to the presence of edge surfaces, diverging from periodic slab trends due to the change in energy of the electronic states. This work provides more realistic, physically meaningful models and offers new insights beyond conventional periodic approaches.

Received 26th May 2025,
Accepted 5th September 2025

DOI: 10.1039/d5nr02231b

rsc.li/nanoscale

1. Introduction

MXenes constitute a class of two-dimensional (2D) transition metal carbides, nitrides, and carbonitrides. This low-dimensional family was discovered back in 2011 by Naguib *et al.*[1] who were able to synthesize Ti_3C_2, the first MXene prototypical example, containing five atomic layers only —excluding terminations (see below). Since then, the number of MXenes has considerably grown and many applications such as in catalysis, biomedicine, and energy storage have been envisaged.[2–4] MXenes are generally synthesized through the selective chemical etching of three-dimensional (3D) ternary layered MAX phases with general $M_{n+1}AX_n$ chemical formula, where M represents an early transition metal, A is an element from groups XIII or XIV, X is either carbon (C) and/or nitrogen (N), and n (ranging from 1 to 4) determines the thickness of the resulting material.[5–7] After the etching process, the formed MXene chemical formula becomes $M_{n+1}X_nT_x$, where T_x represents surface termination groups (functional groups) attached to the MXene basal plane arising from the synthesis conditions. Termination groups typically include –F, –H, –O, and –OH when using hydrofluoric acid as an *in situ* etching agent.[3,4] Note that additional processing or alternative etching can further remove these groups,[8,9] resulting in pristine MXene surfaces, denoted by $M_{n+1}X_n$.[3,10]

From the point of view of physical and chemical properties, MXenes stand out from other 2D materials due to their wide and vast range of properties. Most of them present a metallic character with no band gap in their electronic structure.[11–14] Nevertheless, as expected, their properties strongly depend on their composition, thickness, and surface terminations.[2] Among the various applications of MXenes, the most relevant ones are as materials for electromagnetic interference shielding[15–17] lubrication,[18,19] alkali-ion batteries,[10,20–22] thermo-, electro-, and photocatalysis,[14,23–27] and gas and biosensing.[28,29]

Departament de Ciència de Materials i Química Física & Institut de Química Teòrica i Computacional (IQTCUB), Universitat de Barcelona, c/Martí i Franquès 1-11, 08028 Barcelona, Spain. E-mail: angel.morales@ub.edu

From the theoretical and modelling point of view, the vast majority of studies regarding MXene properties represent these materials by means of periodic models, with a perfect, infinite surface free of defects, except when they are introduced *ad hoc* into the unit cell. While this type of model has provided invaluable physical and chemical insights, one must realize that experimentally synthesized MXenes possess finite sizes and exhibit different morphologies where edges are always present. In fact, only a few works have dealt with the importance of MXene edge effects. Some authors have incorporated edge effects by considering large unit cell models that represent MXene nanoribbons (1D),[30–32] and at least one study has explored quantum dots (0D)[33] generated *via* cutting the periodic model as is usually made to cut graphene structures. These previous works involved studying the edge effects on some physical properties of MXenes, including the importance of edges on the hydrogen evolution reaction by means of MXene nanoribbon models.[34]

Clearly, determining the possible role of MXene edges is still in its infancy, and a more systematic approach is needed to provide more realistic atomistic models from a well-defined procedure. To this end, we propose here a new approach for modelling pristine MXene flakes that resemble those observed in experiments. The approach is based on the well-known Wulff construction,[35] which takes into account the crystal structure, symmetry, and superficial energies of materials to define their likely shapes and minimize the overall model surface energy. This approach has been successfully used by different authors to model oxide nanoparticles of CeO_2, TiO_2, and ZnO, in either their anhydrous or hydroxylated form,[36–41] and metallic systems.[42–44] From the initial Wulff construction-based flake models, a more realistic atomic structure can be obtained by means of density functional theory (DFT) optimization, and this can be subsequently used to study the effect of quantum confinement (QC) and size-dependent properties of interest such as the relative stability, energy formation, and the electronic structure. In the present work, this approach is applied to build and analyse Ti_2C flakes with a broad range of increasing sizes.

2. Building MXene flake models and computational details

To investigate the effect of size and morphology on MXene flakes, we selected Ti_2C as a prototype example in our case study. This selection is motivated by (i) composition, in that a Ti-derived MXene constitutes the workhorse in atomic modelling, and (ii) the 3-layer system of Ti_2C behaves similarly to its 5-layer (Ti_3C_2) counterpart from a physical and chemical point of view, allowing us to reduce the dimensionality and thus optimize the computational cost. The workflow starts by optimizing the structure of the $c(1 \times 1)$ conventional unit cell of ABC-stacked bare Ti_2C featuring two basal planes with (0001) Miller indices (see Fig. 1a). Next, to obtain surface energies necessary to model the Wulff construction, the $c(1 \times 1)$ cell was expanded to a $c(3 \times 3)$ cell and optimized again. From this supercell, several stoichiometric nanoribbons were created along the only two sets of non-equivalent crystallographic planes present, namely $\{10\bar{1}0\}$ and $\{11\bar{2}0\}$. Due to the inherent ABC stacking of bare Ti_2C, there are two non-equivalent types of parallel $(11\bar{2}0)$ planes. By cleaving the MXene through this plane, two different surfaces can be generated, differentiated by the atoms they expose. These are a nonpolar surface exposing Ti and C atoms and a polar surface exposing C atoms on one side of the cut and only Ti atoms on the other side (see Fig. 1c). In the following, these surfaces are denoted as $(11\bar{2}0)$-nonpolar and $(11\bar{2}0)$-polar, respectively. As a result, three different nanoribbons are possible among which one corresponds to cutting along the $(10\bar{1}0)$ plane with a width of 5.7 Å (see Fig. 1d), and two correspond to cutting along the $(11\bar{2}0)$ plane, both with a width of 14.5 Å (see Fig. 1e and f). Once the atomic structure of the three nanoribbons is obtained from geometric optimization as indicated in the next section, the required surface energy (γ) values relative to the periodic MXene model were calculated as

$$\gamma = (E_{\text{nanorib}} - n \cdot E_{Ti_2C\text{–slab}})/2S, \qquad (1)$$

where E_{nanorib} is the total energy of the modelled nanoribbon; $E_{Ti_2C\text{–slab}}$ is the energy of the Ti_2C $c(1 \times 1)$ cell; n stands for the number of Ti_2C units of the nanoribbon relative to the Ti_2C $c(1 \times 1)$ unit cell; and S is the surface area created by the cutting of the $(10\bar{1}0)$ and $(11\bar{2}0)$ surfaces. Note that in order to calculate the $(11\bar{2}0)$-polar surface energy, a dipole correction has been considered in the calculations.

To build binary nanoparticles with defined stoichiometry, one can make use of the freely available computer code developed by González *et al.*[45] or rely on the WulffPack Python library;[46] the latter was chosen herein. Both approaches make use of symmetry and surface energies, which are the necessary components when applying the Wulff construction theorem.[35] A home-made program, using the WulffPack Python library, was developed to generate a series of bare Ti_2C flakes with different sizes, ranging from 18 to 168 units of Ti_2C. At this point, one must realize that the flakes constructed may not exhibit the proper $(Ti_2C)_n$ stoichiometry. To this end, a number of isomers were built removing a C atom from each initial MXene flake model. Due to symmetry reasons, different C atoms can be removed from each flake, and thus, the most stable one should be selected. The different isomers considered for each $(Ti_2C)_n$ flake, and their relative stabilities, are shown in Fig. S1 and Table S1, respectively, of the Supplementary Information (SI). Notably, for all $(Ti_2C)_n$ flakes, the most stable isomer corresponds to that from which the C atom was removed from the flake's vertex position. Consequently, this isomer was chosen to carry out all present studies of the size-dependent properties for all flakes.

Once the bare Ti_2C flakes have been modelled, the effect of surface functionalization with O atoms was further explored. Note in passing that MXenes synthesized *via* HF etching can typically feature mixed terminations, including –OH and –F;

a) Ti_2C

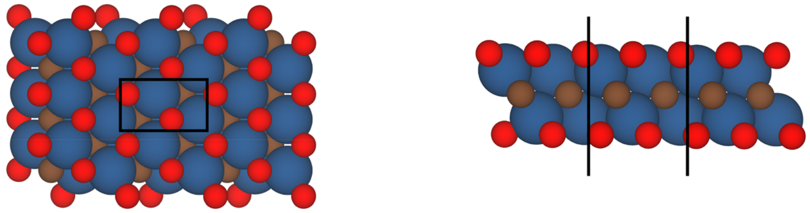

b) Ti_2CO_2

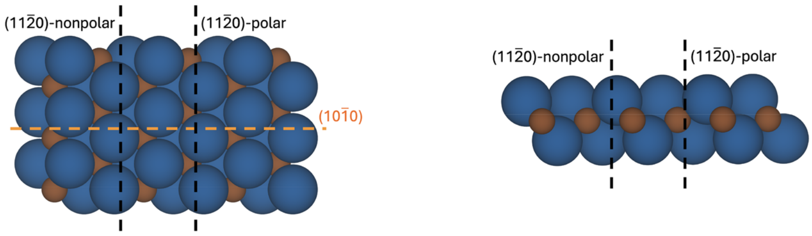

c)

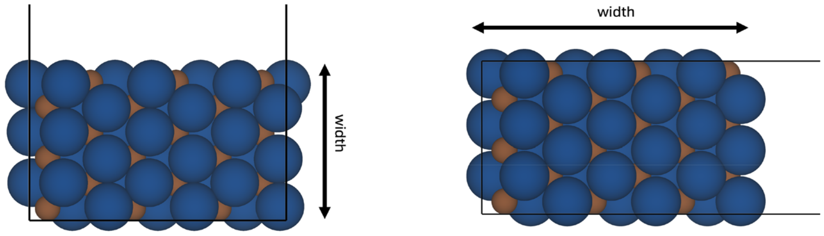

d) (10$\bar{1}$0) Ti_2C e) (11$\bar{2}$0)-nonpolar Ti_2C

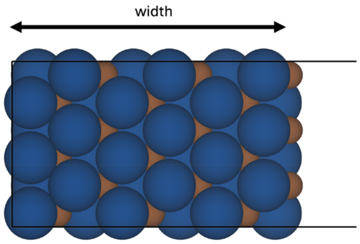

f) (11$\bar{2}$0)-polar Ti_2C

Fig. 1 Top (left-hand panel) and side views (right-hand panel) of (a) bare Ti_2C and (b) Ti_2CO_2 all featuring basal planes with (0001) Miller indices and the *c*(1 × 1) cell marked with black lines. Panel (c) displays the top (left) and side (right) views of the cuttings to generate (d) Ti_2C(10$\bar{1}$0), (e) Ti_2C (11$\bar{2}$0)-nonpolar, and (f) Ti_2C(11$\bar{2}$0)-polar surfaces, which include arrows showing the direction along which the width has been measured. Note that even if the Ti_2C(11$\bar{2}$0)-nonpolar and Ti_2C(11$\bar{2}$0)-polar planes are parallel, they are not equivalent as, due to the ABC stacking of the atomic layers, the atoms they expose are different. The Ti atoms are represented with blue spheres, while the C and O atoms are represented with brown and red spheres, respectively. For (a) and (c), the *c*(1 × 1) cells and the supercells in the remaining figures are marked with black lines.

however, we chose the most common –O termination as a case of study. To this end, we selected $(Ti_2C)_{18}$, $(Ti_2C)_{60}$, and $(Ti_2C)_{126}$ as representative cases. For these three flakes, adsorbed O atoms were placed at each hollow metal site of the (0001) surfaces, as this is the most favourable adsorption site, always assuring the global stoichiometry, leading to a CABCA stacking arrangement.[13,47] We acknowledge that full oxygen termination represents an idealized model, while partial or mixed terminations are more realistic under experimental conditions. Our aim here was to isolate the intrinsic effects of pure oxygen functionalization. Next, the structures of the resulting $(Ti_2CO_2)_{18}$, $(Ti_2CO_2)_{60}$, and $(Ti_2CO_2)_{126}$ flakes were optimized, with the final structures displayed in Fig. 3. To study the possible size-dependent properties of the $(Ti_2CO_2)_n$ flakes, the periodic Ti_2CO_2 slab model (see Fig. 1b), with the same CABCA stacking, has also been considered as a reference of infinite size. It is worth pointing out that the present study focuses on the convergence of flake properties to the periodic slab model limit. Therefore, edge functionalization has not been considered. Note also that, as the flake total surface area is dominated by the basal plane, especially for large flakes, the effect of edge functionalization is likely to represent a small perturbation of the reported trends. Nevertheless, one must also point out that edge functionalization can affect the overall stability of the flakes, as previous experimental findings reveal that flakes can take a maximum amount of oxygen before they decompose.[48] The study of edge functionalization represents an open front that is worth of future studies that specifically address the coverage limit.

The atomic and electronic structures of Ti_2C and Ti_2CO_2 periodic slabs, as well as those of the $(Ti_2C)_n$ and $(Ti_2CO_2)_n$ flakes, and their relative stability, were assessed by means of all-electron DFT-based calculations, carried out with the Fritz-Haber Institute *Ab Initio* Materials Simulation (FHI-AIMS) package.[49] The Perdew–Burke–Ernzerhof (PBE) form[50] of the Generalized Gradient Approximation (GGA) density functional was chosen and scalar relativistic effects were included through the Zeroth-Order Regular Approximation (ZORA).[51,52] This code numerically solves the Kohn–Sham equations by expanding the electron density in a basis set of Numerical Atomic-centered Orbitals (NAOs). From the different sets of NAOs provided by FHI-AIMS, we selected the tier-1/light-grid[53] one, which has a quality similar to that of a triple-ζ plus polarization Gaussian Type Orbitals (GTO) basis set.[54] The lattice vector forces were optimized with an analytical stress tensor.[55]

In all calculations, a threshold self-consistent charge density convergence criterion of 10^{-5} eV was used, and all structural optimizations were reached when atomic forces were below 10^{-3} eV Å^{-1}, using a Gaussian broadening sigma value of 0.01 eV for partial occupancies to speed up convergence. Only for periodic slab calculations, a 7 × 7 × 1 *k*-point mesh[56] was used, dense enough to sample representatively the Brillouin zone, along with a vacuum space of 30 Å in the normal direction to the MXene (0001) surface —the *z*-direction —, large enough to avoid interaction between slab replicas. These periodic calculations were performed to assess convergence trends.

In spite of the fact that previous studies have predicted that the bare Ti_2C material exhibits a magnetic ground state with two ferromagnetic layers coupled antiferromagnetically,[57] all geometry optimizations were performed without accounting for spin-polarization as this has been shown to have a negligible effect on the structural parameters of MXenes.[12,57] However, for a more accurate description of the properties of the investigated flakes, the relative stability and formation energies were studied with and without spin-polarization. Note also that when the periodic Ti_2C (0001) surface is functionalized, the inherent magnetism of Ti_2C is removed.[12,57,58]

To investigate the effect of QC on the properties of these systems, we focus on the averaged coordination number for each species in each MXene flake, the relative stability with respect the periodic slab, the formation energy, the overall energy gap —estimated as the difference between the Kohn–Sham orbital energy of the Highest Occupied Molecular Orbital (HOMO) and the Lowest Unoccupied Molecular Orbital (LUMO)—, the band edge energies, and the possible magnetism of their electronic ground state. The averaged coordination number for each species in each MXene flake was determined by means of a home-made program that employs the well-known Atomic Simulation Environment (ASE)[59] Python library. The relative stability with respect to the periodic slab (ΔE) per formula unit was computed using the following eqn (2):

$$\Delta E = (E_{\text{flake}} - n \cdot E_{\text{Ti}_2\text{C-slab}})/n, \tag{2}$$

where E_{flake} is the total energy of each $(Ti_2C)_n$ flake. On the other hand, the formation energy per formula unit, E_f, was calculated with respect to the most stable bulk phase of each component as:

$$E_f = \left(E_{\text{flake}} - \frac{n}{m}E_{\text{graphite}} - \frac{2n}{l}E_{\text{Ti-hcp}}\right)/n, \tag{3}$$

where E_{graphite} and $E_{\text{Ti-hcp}}$ are the total energies of the unit cells of graphite and Ti metal with a hexagonal close-packed (*hcp*) crystal structure, respectively, and *m* and *l* correspond to the number of atoms in each unit cell of graphite and Ti-*hcp*, respectively.

To estimate the optimal band gap, we used the difference between the HOMO and LUMO states. The limitations of GGA functionals in predicting accurate band gaps arise from their tendency to excessively delocalize electrons.[60,61] Therefore, single-point calculations were performed on PBE-level relaxed structures using the hybrid Heyd–Scuseria–Ernzerhof (HSE06) functional,[62,63] which incorporates a 25% non-local Fock exchange and a range-separation parameter of 0.2 Å^{-1} to account for the short-range interaction term. Previous studies have shown that this hybrid functional is more reliable in describing the electronic structure of these systems than the PBE functional.[12,14,57,64]

Finally, to study the effect of QC on the inherent magnetism, the relative stabilities of each non-spin-polarized and spin-polarized solution were assessed. In particular, we focus on energy differences between the non-spin-polarized, with a closed-shell configuration (NM or non-magnetic), the antiferromagnetic (AFM), and the ferromagnetic (FM) solutions. Note that previous studies have shown that the ground state of Ti_2C MXenes is magnetic with one unpaired electron per magnetic centre mainly localized at surface Ti atoms and with an antiferromagnetic coupling of the two ferromagnetic layers of Ti atoms; for more details, see ref. 12, 57 and 64.

3. Results and discussion

3.1. Bare $(Ti_2C)_n$ flakes with $18 \leq n \leq 168$

From the calculated relative surface energies, γ, of 4.93, 4.63, and 5.79 J m^{-2} for the $(10\bar{1}0)$, $(11\bar{2}0)$-nonpolar, and $(11\bar{2}0)$-polar surfaces, respectively, and employing the Wulff construction, a series of $(Ti_2C)_n$ flakes with $18 \leq n \leq 168$ flakes were constructed. Note that, apart from the most stable (0001) surface corresponding to the basal plane of the MXene, the $(11\bar{2}0)$-nonpolar surface emerges as the most thermodynamically stable one with respect to the periodic Ti_2C model, followed by the $(10\bar{1}0)$ and $(11\bar{2}0)$-polar surfaces. Then, from a morphological point of view, the resulting structure acquires a hexagonal shape as shown, for instance, in the optimized $(Ti_2C)_{60}$ flake with the exposed surfaces appropriately labelled in Fig. 2. From this, and according to the Wulff theorem, it is clear that the most stable $(11\bar{2}0)$-nonpolar surface promotes the largest surface exposure perpendicular to the basal plane, providing a global hexagonal shape to the flake, whereas the expression of the $(10\bar{1}0)$ surface is less prominent, just trimming the hexagon vertices.

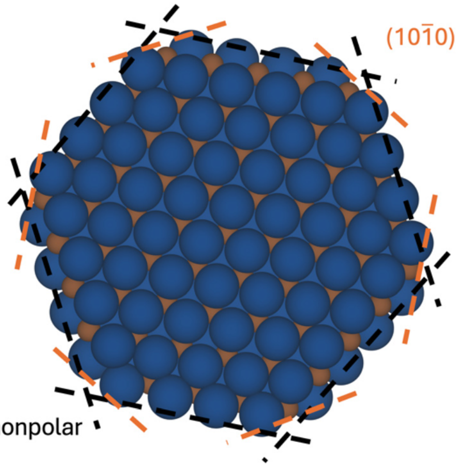

Fig. 2 Top view of the $(Ti_2C)_{60}$ flake obtained from cuts made along the $(10\bar{1}0)$ and $(11\bar{2}0)$-nonpolar planes represented by orange and black dashed lines, respectively, according to the Wulff construction procedure. Colour coding as in Fig. 1.

Fig. 3 shows all optimized $(Ti_2C)_n$ flakes, including side and top views and their size in nm. After optimization, all $(Ti_2C)_n$ flakes remain flat and preserve the ABC stacking arrangement as in the periodic slab models without atoms changing the plane and with an average Ti–C distance of ~2.1 Å regardless of the flake size. Interestingly, this value matches the one obtained when using a periodic slab model.[57,65–67] Here, the size of each $(Ti_2C)_n$ flake was estimated using the planar diameter, $\varnothing$, estimated as the distance between opposing $(10\bar{1}0)$ surfaces. The diameters shown in Fig. 3 indicate that the sizes of $(Ti_2C)_n$ flakes range from 1.01 to 3.65 nm.

On the other hand, the sizes of $(Ti_2C)_n$ flakes influence directly the average atom coordination, as shown in Fig. 4, which will necessarily have an impact on their chemistry as indicated by experimental evidence that capping the MXene edge flakes with polyanionic salts reduces the oxidation rate of the synthesized flakes in aqueous solution.[68] It is worth highlighting that in the periodic Ti_2C slab, due to the *hcp* arrangement of Ti atoms, each Ti atom has six Ti in-plane neighbours and three Ti out-of-plane neighbours, with C atoms occupying the octahedral holes in the *hcp* lattice; hence the coordination number of Ti and C atoms in the periodic slab is 12 and 6, respectively. For a better visual understanding of the atomic coordination, a simplified scheme is shown in Fig. S2 in the SI. The larger the flake size, the closer is the average coordination of Ti and C atoms slowly converging to the periodic slab values.

Regarding the relative stability of the $(Ti_2C)_n$ flakes with respect to the periodic slab model, Fig. 5 (left-hand panel) displays the trend as a function of flake size. This Fig. 5 shows a characteristic asymptotic trend, where the total energy per formula unit decreases towards the total energy of the periodic slab as the Ti_2C flake size increases. To better understand the energetic stability of $(Ti_2C)_n$ flakes, ΔE, relative to that of the periodic slab, $E_{Ti_2C-slab}$, we rely on the Spherical Cluster Approximation (SCA),[69] where, in principle, one can approximate the relative stability of a cluster with respect to the bulk as

$$\Delta E = E_{\text{bulk}} + \sum_{i=1} a_i \cdot (n^{-\alpha})^i. \qquad (4)$$

In the SCA framework, where one is interested in the convergence of ΔE of finite clusters or nanoparticles to the 3D bulk limit, one has $\alpha = 1/3$, reflecting the area to volume ratio,[70] a_i is the fitting parameter, with the first term ($i = 1$) dominating the fit and the remaining terms ($i > 1$) accounting for the particularities of each system, such as surface stress and edge energy contributions.[71–73] In the present case, the periodic limit is a 2D system and thus $\alpha = 1/2$, and here E_{bulk} corresponds to the energy of the periodic slab, $E_{Ti_2C-slab}$. Further details and the fitting parameters of the trends from the plot in the left-hand panel of Fig. 5 are provided in Table S2 in the SI.

Note that, to avoid any bias arising from the choice of a particular solution in DFT calculations, the relative stabilities were calculated for the NM and AFM flakes with respect to the

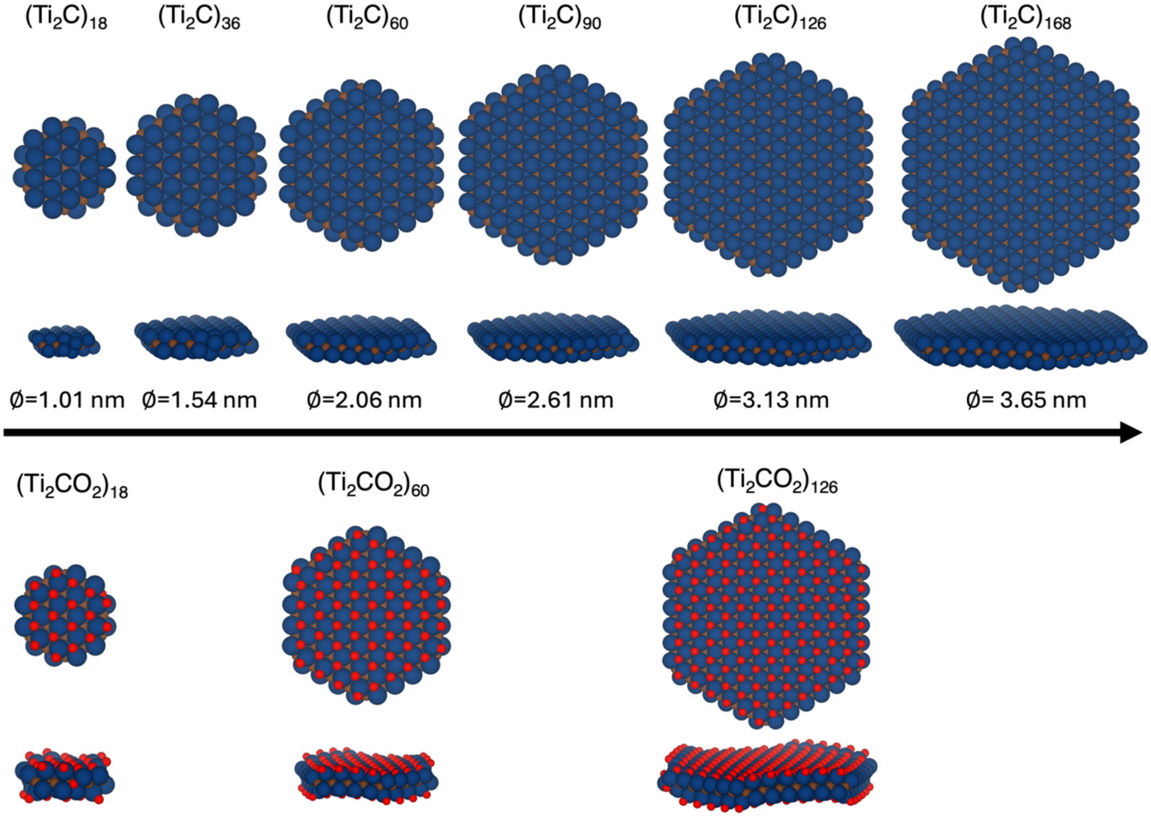

Fig. 3 Top and side views of each optimized and stoichiometric $(Ti_2C)_n$ flake, n = 18–168, including their planar diameter, ∅, in nm, and those of the O-covered $(Ti_2CO_2)_{18}$, $(Ti_2CO_2)_{60}$, and $(Ti_2CO_2)_{126}$ flakes. Colour coding as in Fig. 1.

NM and AFM periodic slabs, respectively, and both results are included in Fig. 5. This figure clearly shows that the calculations lead to the same trend whether or not spin-polarization is included. Nevertheless, except for the smallest $(Ti_2C)_{18}$ flake, the relative stability of AFM flakes is systematically closer relative to that corresponding to the AFM ground state solution for the periodic slab than the one for the NM solution. It is worth highlighting that for the $(Ti_2C)_{18}$ flake, due to the QC effect, the relative stability with respect the periodic slab when the AFM solution is taken into account lies above the NM one by 0.1 eV per formula unit. Note also that for $n > 18$, this energy difference per formula unit increases as the flake size increases.

Similar trends are found for the formation energy of the most stable isomer per chemical unit, as shown in Fig. 5 (right-hand panel). The formation energy decreases towards the periodic slab value with an asymptotic behaviour. Note that the fitting curves are also based on the SCA. This formation energy has also been calculated for the NM and AFM solutions; the AFM E_f is systematically more stable than the NM one for all-sizes of $(Ti_2C)_n$ flakes. Here, the QC effect for the $(Ti_2C)_{18}$ flake is not large enough to position the NM E_f below the AFM one. In addition, the difference in formation energies between the AFM and NM solutions becomes larger as the flake size increases. Again, the general trend of the formation energies remains qualitatively the same regardless of the magnetic solution. We found that the formation energies of periodic Ti_2C are −0.16 eV (AFM) and −0.01 eV (NM) per Ti_2C unit. The formation energies of the flakes converge toward these values as the size increases, deviating by approximately 0.2–0.3 eV for the largest systems studied, indicating progressive stabilization with increasing size. The fitting parameters corresponding to the formation energies in the right-hand panel of Fig. 5 are presented in Table S2 in the SI.

Next, we analysed the effect of flake size on the electronic structure. The energy gap was calculated from the HOMO–LUMO difference as computed with the PBE and HSE06 functionals. Both AFM and NM solutions have been considered in the calculations with the PBE functional and, in both cases, the electronic gap is zero except for the $(Ti_2C)_{18}$ flake for which the QC effect opens a nearly negligible gap of 0.1 eV in the AFM solution. This finding is in agreement with the gap of the AFM solution for the periodic slab also leading to a null value.[12] This is also the case for the NM solution where PBE results are also in line with the estimated zero energy gap of the NM periodic slab. Overall, all calculations indicate that the QC effect do not have a noticeable effect on the electronic structure of Ti_2C flakes. To further confirm this conclusion, calculations were carried out using the hybrid HSE06 functional and considering the NM solution. In all cases, the

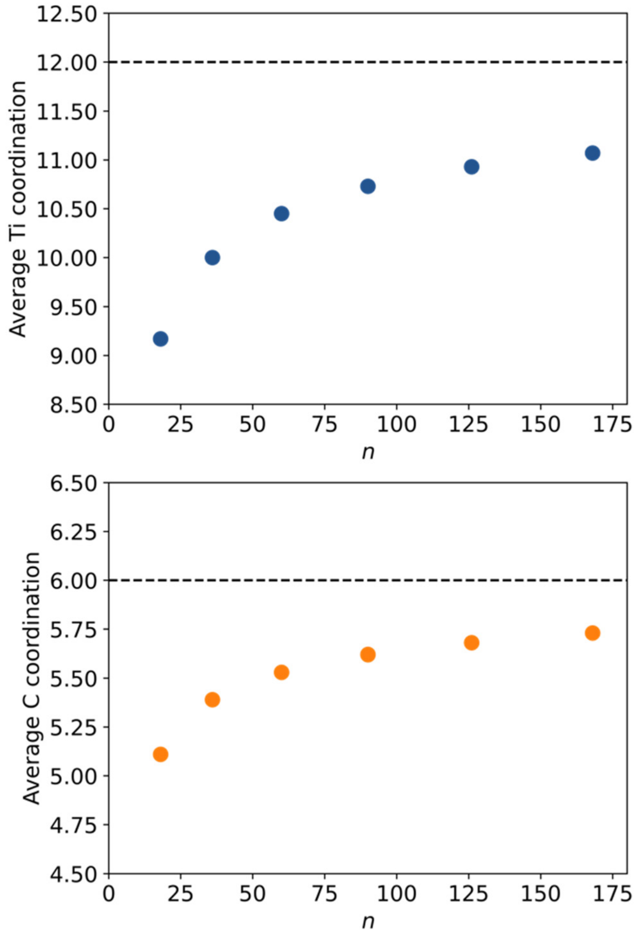

Fig. 4 Average Ti coordination (top panel) and C coordination (bottom panel) for each studied Ti_2C flake as a function of the number of Ti_2C units, n. The dashed black lines correspond to the periodic model values.

energy gap becomes at most 0.1 eV. However, as the flake size increases, the QC effects decrease and, as a consequence, the energy gap becomes zero, thus matching the value obtained for the periodic slab with the HSE06 functional, which is zero for both NM and AFM solutions.[12] For a more visual depiction, the representation of the charge density of the HOMO and LUMO levels is shown in Fig. S3 in the SI. These results show a delocalized character of the charge density, delocalized on the centre and edges of the flake.

Additionally, further insights into the electronic structure can be obtained by analysing the energy of the band edges. Fig. 6 presents the estimated band edge positions for all flakes, calculated using Kohn–Sham values. These values were determined for both PBE and HSE06 functionals. For the former, AFM and NM solutions have been taken into account, whereas for the latter, only NM solutions were considered for HSE06. Although QC does not affect the energy gap, it significantly influences the positions of the Kohn–Sham energy levels. Specifically, these levels become increasingly negative as the size of the $(Ti_2C)_n$ system increases, approaching the slab limits which, for the Valence Band Maximum (VBM), are −3.7 eV (AFM at PBE), −4.0 eV (NM at PBE), and −4.3 eV (NM at HSE06), and for the Conduction Band Minimum (CBM) are −3.5 eV (AFM at PBE), −4.0 eV (NM at PBE), and −4.0 eV (NM at HSE06). Note that for the PBE-AFM band edges (middle panel in Fig. 6), a small deviation of the data is observed due to the excessive electronic delocalization typical of the GGA functionals when dealing with some *d*-electron localization in the AFM solution, as previously reported.[12,57,64] A more detailed picture of the described electronic structure can be obtained from the Density of States (DOS) plots shown in Fig. S4 in the SI. While the DOS in 0D systems consists of discrete energy levels rather than a continuous distribution, we present these plots to monitor the emergence, broadening,

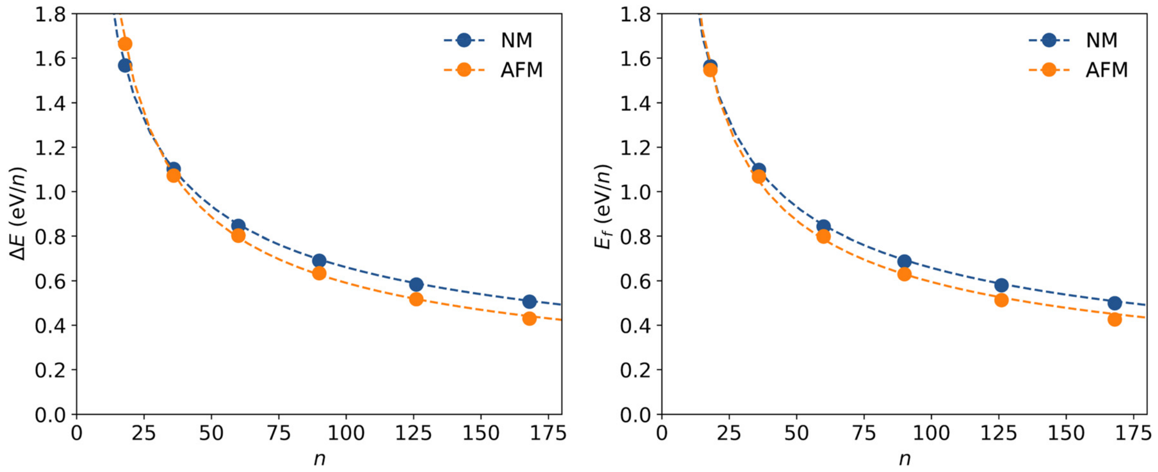

Fig. 5 Relative stability of the most stable isomer on the periodic surface per formula unit n, ΔE in eV/n, given per chemical unit (left-hand panel) and formation energy, E_f in eV/n, (right-hand panel) for the NM and AFM solutions of each $(Ti_2C)_n$, n = 18–168 flake, as a function of the number of Ti_2C units, n. The ΔE and E_f values were calculated using eqn (2) and (3), respectively. The dashed lines correspond to fitting curves of SCA, whose fitting parameters are presented in Table S2 in the SI.

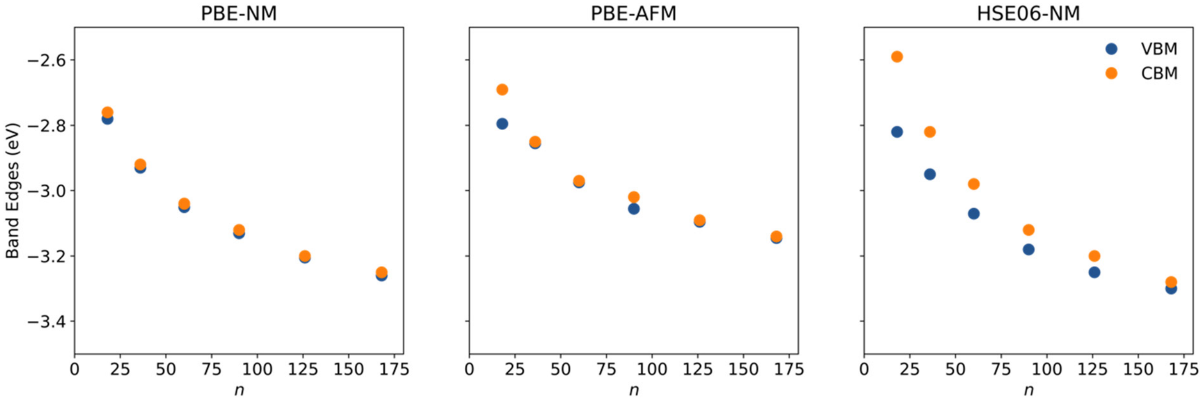

Fig. 6 Band edges for the most stable isomer of each $(Ti_2C)_n$, n = 18–168 flake, and evolution of the Valence Band Maximum (VBM) and the Conduction Band Minimum (CBM) for the PBE NM (left-hand panel) and AFM solutions (central panel) and the HSE06 NM solution (right-hand panel) as a function of n.

and shifting of edge-related states as the flake size increases. This approach allows us to qualitatively assess trends in electronic structure evolution and compare them to periodic behavior. Analysis of these plots shows that all the bare $(Ti_2C)_n$ flakes exhibit a general gapless metallic electronic structure regardless of the functional used (PBE or HSE6). On the other hand, $(Ti_2CO_2)_n$ flakes display a small energy gap, again regardless of the functional used.

For each flake, we analysed the energy difference between the three magnetic configurations as done for the bare periodic Ti_2C MXene in previous studies.[12,57,64] Table 1 summarizes the normalized PBE energy differences (ΔE_{AFM-NM} and ΔE_{AFM-FM}) per number of Ti_2C units for each Ti_2C flake. The results reveal that for all modelled flakes, ΔE_{AFM-NM} consistently adopts negative values, indicating that the AFM solution lies below the NM one. This clearly shows that the magnetic ground state of the periodic Ti_2C slab is preserved even after edge cutting leading to finite flakes. Despite these Ti_2C flakes possessing a magnetic ground state, the influence of QC on the magnetic properties is noticeable, promoting a size-dependent behaviour on the ΔE_{AFM-NM}, monotonically increasing the stability of the AFM solution relative to the NM one as the flake size increases and nicely converging towards a periodic slab value of −143 meV/n.[12,57,64] Further analysis of the ΔE_{AFM-FM} values in Table 1 also reveals size-dependent behaviour due to the QC. For flakes with $n < 90$ Ti_2C units, the ΔE_{AFM-FM} values are less than $|10|$ meV/n, indicating a negligible energy difference. This suggests that, at these sizes, AFM and FM configurations are energetically competitive. On the other hand, for flakes with $n \geq 90$ Ti_2C units, the ΔE_{AFM-FM} values are negative and indicate that the AFM solution lies below the FM one, being energetically favoured, and flakes beyond this size adopt an AFM electronic ground state. Again, these ΔE_{AFM-FM} values converge towards a value of −28 meV/n, corresponding to the periodic slab model.[12,57,64] These findings shed light on the size-dependent magnetic properties of Ti_2C flakes and provide insights into the retention of AFM behaviour in reduced-dimensional MXene systems.

Finally, electrostatic potential isosurfaces were computed employing the HSE06 functional to assess spatial variations in the reactivity of flakes with size. As shown in Fig. S5 in the SI, highly negative potential regions are found at the edges, consistent with enhanced chemical reactivity of the edges.

Table 1 Energy difference between the AFM and either NM or FM solutions (ΔE_{AFM-NM} and ΔE_{AFM-FM}, respectively) per formula unit, n, for the scrutinized $(Ti_2C)_n$ and $(Ti_2CO_2)_n$ flakes in meV/n as predicted from calculations using the PBE functional. The ΔE_{AFM-NM} negative values indicate a magnetic ground state; the ΔE_{AFM-FM} negative values denote that the AFM solution is more stable than the FM one

Flake	n	ΔE_{AFM-NM}	ΔE_{AFM-FM}
Ti_2C	18	−18	1
	36	−30	4
	60	−43	−5
	90	−57	−12
	126	−67	−14
	168	−74	−19
Ti_2CO_2	18	0	0
	60	0	0
	126	0	0

3.2. Effect of O-termination on the basal plane

Herein, we explored the effect of the basal plane functionalization by O atoms on the properties of Ti_2C flakes. To this end, $(Ti_2CO_2)_{18}$, $(Ti_2CO_2)_{60}$, and $(Ti_2CO_2)_{126}$ were selected as representative examples. The O atoms were placed on both sides of the flake's basal planes and initially at hollow-metal sites. After geometry optimization, the CABCA stacking remains unchanged. However, the side view in Fig. 3 shows a clear bending deformation of the plane Ti_2C flake due to the functionalization effect. The calculated deformation energy with respect to the planar geometry of Ti_2CO_2 flakes per formula unit is the same for the three considered flakes and is around −0.3 eV/n. The bending observed in the O-functionalized Ti_2C flakes (Ti_2CO_2) can be attributed to surface stress introduced by the terminal oxygen atoms. These groups distort the local bonding geometry, especially at the edges, and generate an internal strain that favors non-planar geometries. Additionally, the electronegativity imbalance between the Ti and O atoms could induce a small surface dipole, which can further destabilize the flat configuration and promote the bending as the flake minimizes its electrostatic energy. This effect is absent in pristine Ti_2C flakes, which maintain planar structures due to their higher structural symmetry and lack of dipolar interactions. Consequently, the bending deformation stabilizes the $(Ti_2CO_2)_n$ flake regardless of its size. The average interatomic distances resulting from geometry optimization are 2.1, 2.1, and 2.2 Å for $(Ti_2CO_2)_{18}$, $(Ti_2CO_2)_{60}$, and $(Ti_2CO_2)_{126}$, respectively. These values are similar to the size of the corresponding Ti_2CO_2 periodic slab, which is 2.2 Å. Similarly, the Ti–O averaged distance for the three slabs is 1.9, 2.0, and 2.0 Å for $(Ti_2CO_2)_{18}$, $(Ti_2CO_2)_{60}$, and $(Ti_2CO_2)_{126}$, respectively, again similar to the bond length value in the periodic slab of 2.0 Å. It is worth noting that even though this structural bending is not captured by the averaged interatomic distances, it extends upward towards the surface where the O-termination is exposed and, by symmetry and inherent stacking, downward towards the surface where the O-termination is exposed on the opposite surface. In fact, the highest (lowest) vertical position of an O atom is 0.4, 0.7, and 1.0 Å (−0.3, −1.2, and −1.2 Å) above (below) the O-plane for $(Ti_2CO_2)_{18}$, $(Ti_2CO_2)_{60}$, and $(Ti_2CO_2)_{126}$, respectively.

The effect of O functionalization on the electronic structure is noticeable even if the PBE ground state is NM as in the periodic slab. In fact, the PBE-calculated energy gap values for the NM solution are of 0.1, 0.1, and 0.0 eV for $(Ti_2CO_2)_{18}$, $(Ti_2CO_2)_{60}$, and $(Ti_2CO_2)_{126}$, respectively, which are significantly different from the 0.4 eV value corresponding to the periodic slab model, as estimated in previous works.[13] Since the PBE functional is known to significantly underestimate the band gap of the insulator, the NM solution was also computed using the HSE06 functional. The HSE06 values show the same trend with decreasing values of 0.7, 0.2, and 0.1 eV for $(Ti_2CO_2)_{18}$, $(Ti_2CO_2)_{60}$, and $(Ti_2CO_2)_{126}$, respectively. This implies that, as the size of the Ti_2CO_2 flake increases, the energy gap closes itself, which is unexpected as the QC effect decreases with increasing size. The reason behind this behaviour is not simple since the optical band gap for the periodic slab predicted by the HSE06 functional is 1.0 eV. Therefore, other effects beyond QC must be playing a role. In fact, the divergence between the electronic gap of the finite-size flakes and the reference periodic slab models has been documented in previous studies by Hong *et al.*[31] and Zhou *et al.*[32] using MXene nanoribbon models. These authors unveiled the influence of edge effects on the electronic structure of Ti_2CO_2 nanoribbons, with the appearance of electronic states in the middle of the band gap. These energetically downshift the CBM, narrowing the band gap as the nanoribbon width decreases. Notably, we represented the charge density of the HOMO and LUMO eigenstates (see Fig. S3 in the SI). These states appear to be delocalized over the centre of the flake and not localized in the edges, implying that the edge surface formation only influences the energy position of the HOMO and LUMO orbitals and not the nature of these orbitals, narrowing the gap as the flake size increases. In addition, a comparison between the pristine Ti_2C and Ti_2CO_2 flakes shows that the HOMO and LUMO levels of the Ti_2CO_2 flakes seem to be more localized than Ti_2C ones.

Finally, regarding the magnetic properties of the considered Ti_2CO_2 flakes, Table 1 also presents the $\Delta E_{\mathrm{AFM-NM}}$ and $\Delta E_{\mathrm{AFM-FM}}$ values for these flakes as obtained from calculations with the PBE functional. All these calculated values are zero, inferring that each Ti_2C flake loses its magnetic ground state when O atoms functionalize both (0001) surfaces, acquiring an NM ground state, which fully agrees with the results obtained for the periodic Ti_2CO_2 slab model, using either PBE or HSE06 functionals.[57,58]

4. Conclusions

We investigated the properties of realistically shaped Ti_2C MXene flakes, obtained *via* the Wulff construction to reflect experimental morphologies, using DFT-based calculations. Structural, energetic, electronic, and magnetic features were analyzed in flakes of increasing size, including oxygen-functionalized variants. The flakes adopt a hexagonal shape dominated by a thermodynamically stable $(11\bar{2}0)$-nonpolar surface with a few $(10\bar{1}0)$ surfaces trimming the vertices of the hexagon. Indeed, all flakes approach the structural characteristics of the periodic slab, with consistent Ti–C distances of ∼2.1 Å across all sizes. The relative stability of the bare flakes approaches that of the infinite slab with increasing size, and the AFM configuration remains the ground state, especially for flakes with $n \geq 90$, where it becomes more energetically favored over NM and FM solutions. QC has a marked influence on smaller flakes, affecting their stability and magnetic properties, but in larger systems its impact diminishes.

Electronic structure calculations show that all Ti_2C flakes remain gapless within the PBE approach, with minimal size-dependent QC effects. On the other hand, calculations with the hybrid HSE06 functional yield small band gaps that vanish with size, reproducing the metallic character of the periodic model. Notably, band edge positions shift with size, suggesting tunability for optoelectronic applications. In addition, the electrostatic potential isosurface predicts that the edge formation promotes enhanced reactivity along the edges. Upon O functionalization, the flakes become NM and slightly bent, with narrowing size-dependent band gaps that deviate from slab behavior due to edge-induced state shifts.

Overall, this study has highlighted the relevance of flake size and edge effects with respect to the stability and electronic behavior of MXene materials. We hope that the realistic, physically meaningful models presented in this work will contribute to better understanding of the properties of the experimentally synthesized MXene flakes and reveal new aspects of the chemistry of these materials not easily reachable by periodic models, either of extended surfaces or nanoribbons.

Conflicts of interest

There are no conflicts to declare.

Data availability

The data supporting this article have been included as part of the SI. Supplementary information is available. See DOI: https://doi.org/10.1039/d5nr02231b.

Specific data files (files or atomic models) related to this study are available upon request from the corresponding author.

Acknowledgements

This study was supported by the Spanish Ministerio de Ciencia e Innovación and Agencia Estatal de Investigación (AEI) MCIN/AEI/10.13039/501100011033 through projects PID2021-126076NB-I00, TED2021-129506B-C22, CNS2024-154493, and PID2024-159906NB-I00 la Unidad de Excelencia María de Maeztua CEX2021-001202-M granted to the IQTCUB and, in part, from COST Action CA18234 and Generalitat de Catalunya 2021SGR00079. Some of the calculations were carried out using the supercomputers of the Consorci de Serveis Universitaris de Catalunya (CSUC). N. G.-R. thanks the Generalitat de Catalunya for a predoctoral contract 2022 FISDU 00106. F. V. is thankful for the ICREA Academia Award 2023 Ref. Ac2216561.

References

1 M. Naguib, M. Kurtoglu, V. Presser, J. Lu, J. Niu, M. Heon, L. Hultman, Y. Gogotsi and M. W. Barsoum, *Adv. Mater.*, 2011, **23**, 4248–4253.

2 Y. Gogotsi and B. Anasori, *ACS Nano*, 2019, **13**, 8491–8494.

3 M. Naguib, V. N. Mochalin, M. W. Barsoum and Y. Gogotsi, *Adv. Mater.*, 2014, **26**, 992–1005.

4 A. VahidMohammadi, J. Rosen and Y. Gogotsi, *Science*, 2021, **372**, 1165.

5 J. C. Lei, X. Zhang and Z. Zhou, *Front. Physiol.*, 2015, **10**, 276–286.

6 M. Khazaei, A. Mishra, N. S. Venkataramanan, A. K. Singh and S. Yunoki, *Curr. Opin. Solid State Mater. Sci.*, 2019, **23**, 164–178.

7 G. Deysher, C. E. Shuck, K. Hantanasirisakul, N. C. Frey, A. C. Foucher, K. Maleski, A. Sarycheva, V. B. Shenoy, E. A. Stach, B. Anasori and Y. Gogotsi, *ACS Nano*, 2020, **14**, 204–217.

8 I. Persson, J. Halim, H. Lind, T. W. Hansen, J. B. Wagner, L.-Å. Näslund, V. Darakchieva, J. Palisaitis, J. Rosen and P. O. Å. Persson, *Adv. Mater.*, 2019, **31**, 1805472.

9 V. Kamysbayev, M. Filatov, X. Hu, X. Rui, F. Lagunas, D. Wang, S. K. Fullon, A. Sarycheva, A. Srivastava, M. J. May, L. Balents, Y. Gogotsi and D. V. Talapin, *Science*, 2020, **369**, 979–983.

10 B. Anasori and Y. Gogotsi, *2D Metal Carbides and Nitrides (MXenes)*, ed. B. Anasori and Y. Gogotsi, Springer, 2019.

11 M. Khazaei, M. Arai, T. Sasaki, C.-Y. Chung, N. S. Venkataramanan, M. Estili, Y. Sakka and Y. Kawazoe, *Adv. Funct. Mater.*, 2013, **23**, 2185–2192.

12 N. García-Romeral, Á. Morales-García, F. Viñes, I. de P. R. Moreira and F. Illas, *Phys. Chem. Chem. Phys.*, 2023, **25**, 31153–31164.

13 D. Ontiveros, F. Viñes and C. Sousa, *J. Mater. Chem. A*, 2023, **11**, 13754–13764.

14 D. Ontiveros, S. Vela, F. Viñes and C. Sousa, *Energy Environ. Mater.*, 2024, **7**, e12774.

15 F. Shahzad, M. Alhabeb, C. B. Hatter, B. Anasori, S. M. Hong, C. M. Koo and Y. Gogotsi, *Science*, 2016, **353**, 1137–1140.

16 T. Yun, H. Kim, A. Iqbal, Y. S. Cho, G. S. Lee, M.-K. Kim, S. J. Kim, D. Kim, Y. Gogotsi, S. O. Kim and C. M. Koo, *Adv. Mater.*, 2020, **32**, e1906769.

17 A. Iqbal, F. Shahzad, K. Hantanasirisakul, M.-K. Kim, J. Kwon, J. Hong, H. Kim, D. Kim, Y. Gogotsi and C. M. Koo, *Science*, 2020, **369**, 446–450.

18 G. Boidi, J. C. F. de Queiróz, F. J. Profito and A. Rosenkranz, *ACS Appl. Nano Mater.*, 2023, **6**, 729–737.

19 A. Rosenkranz, M. C. Righi, A. V. Sumant, B. Anasori and V. N. Mochalin, *Adv. Mater.*, 2023, **35**, 2207757.

20 F. Bu, M. M. Zagho, Y. Ibrahim, B. Ma, A. Elzatahry and D. Zhao, *Nano Today*, 2020, **30**, 100803.

21 Q. Tang, Z. Zhou and P. Shen, *J. Am. Chem. Soc.*, 2012, **134**, 16909–16916.

22 Y. Yang, J. Chen, J. Tang, F. Xing and M. Yao, *J. Phys. Chem. C*, 2021, **125**, 21453–21459.

23 D. Dolz, R. De Armas, P. Lozano-Reis, Á. Morales-García, F. Viñes, R. Sayós and F. Illas, *ChemCatChem*, 2024, **16**, e202400122.

24 R. Ramírez Grau, P. Garcia-Aznar, G. Sastre, S. Goberna-Ferrón, O. Pavel, A. Tirsoaga, B. Cojocaru, D. G. Popescu, V. I. Parvulescu, A. Primo and H. García, *J. Am. Chem. Soc.*, 2025, **147**, 3315–3332.

25 H. Zhou, Z. Chen, E. Kountoupi, A. Tsoukalou, P. M. Abdala, P. Florian, A. Fedorov and C. R. Müller, *Nat. Commun.*, 2021, **12**, 5510.

26 L. Meng, L.-K. Yan, F. Viñes and F. Illas, *J. Mater. Chem. A*, 2024, **12**, 7856–7874.

27 J. D. Gouveia, G. Novell-Leruth, P. M. L. S. Reis, F. Viñes, F. Illas and J. R. B. Gomes, *ACS Appl. Bio Mater.*, 2020, **3**, 5913–5921.

28 K. Xie, J. Wang, S. Xu, W. Hao, L. Zhao, L. Huang and Z. Wei, *Mater. Des.*, 2023, **228**, 111867.

29 J. D. Gouveia, G. Novell-Leruth, F. Viñes, F. Illas and J. R. B. Gomes, *Appl. Surf. Sci.*, 2021, **544**, 148946.

30 S. Zhao, W. Kang and J. Xue, *J. Mater. Chem. C*, 2015, **3**, 879.

31 L. Hong, R. F. Klie and S. Öğüt, *Phys. Rev. B*, 2016, **93**, 115412.

32 Y. Zhou, K. Luo, X. Zha, Z. Liu, X. Bai, Q. Huang, Z. Guo, C.-T. Lin and S. Du, *J. Phys. Chem. C*, 2016, **120**, 17143–17152.

33 B. Vénosová and F. Karlický, *Nanoscale Adv.*, 2023, **5**, 7067–7076.

34 X. Yang, N. Gao, S. Zhou and J. Zhao, *Phys. Chem. Chem. Phys.*, 2018, **20**, 19390.

35 G. Wulff, *Z. Kristallogr.*, 1901, **34**, 449–530.

36 A. S. Barnard and P. Zapol, *Phys. Rev. B: Condens. Matter Mater. Phys.*, 2004, **70**, 235403.

37 C. Loschen, A. Migani, S. T. Bromley, F. Illas and K. M. Neyman, *Phys. Chem. Chem. Phys.*, 2008, **10**, 5730.

38 A. Migani, K. M. Neyman, F. Illas and S. T. Bromley, *J. Chem. Phys.*, 2009, **131**, 064701.

39 F. Viñes, O. Lamiel-Garcia, F. Illas and S. T. Bromley, *Nanoscale*, 2017, **9**, 10067–10074.

40 O. Lamiel-Garcia, K. C. Ko, J. Y. Lee, S. T. Bromley and F. Illas, *J. Chem. Theory Comput.*, 2017, **13**, 1785–1793.

41 M. Recio-Poo, Á. Morales-García, F. Illas and S. T. Bromley, *Nanoscale*, 2024, **16**, 8975–8985.

42 L. Vega, J. Ruvireta, F. Viñes and F. Illas, *J. Chem. Theory Comput.*, 2018, **14**, 395–403.

43 J. Ruvireta, L. Vega and F. Viñes, *Surf. Sci.*, 2017, **664**, 45–49.

44 D. Vázquez-Parga, A. Fernández-Martínez and F. Viñes, *J. Chem. Theory Comput.*, 2023, **19**, 8285–8292.

45 D. González, B. Camino, J. Heras-Domingo, A. Rimola, L. Rodríguez-Santiago, X. Solans-Monfort and M. Sodupe, *J. Phys. Chem. C*, 2020, **124**, 1227–1237.

46 J. M. Rahm and P. Erhart, *J. Open Source Softw.*, 2020, **5**, 1944.

47 M. Keyhanian, D. Farmanzadeh, Á. Morales-García and F. Illas, *J. Mater. Chem. A*, 2022, **10**, 8846–8855.

48 I. Persson, J. Halim, T. W. Hansen, J. B. Wagner, V. Darakchieva, J. Palisaitis, J. Rosen and P. O. Å. Persson, *Adv. Funct. Mater.*, 2020, **30**, 1909005.

49 V. Blum, R. Gehrke, F. Hanke, P. Havu, V. Havu, X. Ren, K. Reuter and M. Scheffler, *Comput. Phys. Commun.*, 2009, **180**, 2175–2196.

50 J. P. Perdew, K. Burke and M. Ernzerhof, *Phys. Rev. Lett.*, 1996, **77**, 3865.

51 C. Chang, M. Pelissier and P. Durand, *Phys. Scr.*, 1986, **34**, 394–404.

52 E. van Lenthe, E. J. Baerends and J. G. Snijders, *J. Chem. Phys.*, 1994, **101**, 9783–9792.

53 V. Havu, V. Blum, P. Havu and M. Scheffler, *J. Comput. Phys.*, 2009, **228**, 8367–8379.

54 F. Viñes and F. Illas, *J. Comput. Chem.*, 2017, **38**, 523–529.

55 F. Knuth, C. Carbogno, V. Atalla, V. Blum and M. Scheffler, *Phys. Commun.*, 2015, **190**, 33–50.

56 H. J. Monkhorst and J. D. Pack, *Phys. Rev. B: Condens. Matter Mater. Phys.*, 1976, **13**, 5188.

57 N. García-Romeral, Á. Morales-García, F. Viñes, I. de P. R. Moreira and F. Illas, *J. Phys. Chem. C*, 2023, **127**, 3706–3714.

58 Y. Xie and P. R. C. Kent, *Phys. Rev. B: Condens. Matter Mater. Phys.*, 2013, **87**, 235441.

59 A. H. Larsen, J. J. Mortensen, J. Blomqvist, I. E. Castelli, R. Christensen, M. Dułak, J. Friis, M. N. Groves, B. Hammer, C. Hargus, E. D. Hermes, P. C. Jennings, P. B. Jensen, J. R. Kermode, J. R. Kitchin, E. L. Kolsbjerg, J. Kubal, K. Kaasbjerg, S. Lysgaard, J. B. Maronsson, T. Maxson, T. Olsen, L. Pastewka, A. Peterson, C. Rostgaard, J. Schiøtz, O. Schütt, M. Strange, K. S. Thygesen, T. Vegge, L. Vilhelmsen, M. Walter, Z. Zeng and K. W. Jacobsen, *J. Phys.: Condens. Matter*, 2017, **29**, 273002.

60 I. de P. R. Moreira, F. Illas and R. L. Martin, *Phys. Rev. B: Condens. Matter Mater. Phys.*, 2002, **65**, 155102.

61 Á. Morales-García, R. Valero and F. Illas, *J. Phys. Chem. C*, 2017, **121**, 18862–18866.

62 J. Heyd, G. E. Scuseria and M. Ernzerhof, *J. Chem. Phys.*, 2003, **118**, 8207–8215.

63 X. Ren, P. Rinke, V. Blum, J. Wieferink, A. Tkatchenko, A. Sanfilippo, K. Reuter and M. Scheffler, *New J. Phys.*, 2012, **14**, 053020.

64 N. García-Romeral, Á. Morales-García, F. Viñes, I. de P. R. Moreira and F. Illas, *Phys. Chem. Chem. Phys.*, 2023, **25**, 17116–17127.

65 P. Lv, Y. L. Li and J. F. Wang, *Phys. Chem. Chem. Phys.*, 2020, **22**, 11266–11272.

66 Q. Wan, S. Li and J. B. Liu, *ACS Appl. Mater. Interfaces*, 2018, **10**, 6369–6377.

67 M. Sternik and U. D. Wdowik, *Phys. Chem. Chem. Phys.*, 2018, **20**, 7754–7763.

68 V. Natu, J. L. Hart, M. Sokol, H. Chiang, M. L. Taheri and M. W. Barsoum, *Angew. Chem., Int. Ed.*, 2019, **58**, 12655–12660.

69 R. Johnson, *Masters Series in Physics and Astronomy in Atomic and Molecular Clusters*, Taylor and Francis, 1st edn, 2002.

70 Á. Morales-García, A. Macià Escatllar, F. Illas and S. T. Bromley, *Nanoscale*, 2019, **11**, 9032.

71 A. S. Barnard and P. Zapol, *Phys. Rev. B: Condens. Matter Mater. Phys.*, 2004, **70**, 235403.

72 A. S. Barnard and L. A. Curtiss, *Nano Lett.*, 2005, **5**, 1261–1266.

73 O. Lamiel-Garcia, A. Cuko, M. Calatayud, F. Illas and S. T. Bromley, *Nanoscale*, 2017, **9**, 1049.